

Research Article

Molecular Dynamics Simulation of the Cu/Au Nanoparticle Alloying Process

Linxing Zhang,¹ Qibin Li ,² Sen Tian ,^{3,4} and Guang Hong⁵

¹College of Aerospace Engineering, Chongqing University, Chongqing 400044, China

²Key Laboratory of Low-Grade Energy Utilization Technologies & Systems, Ministry of Education, College of Energy and Power Engineering, Chongqing University, Chongqing 400044, China

³State Key Laboratory of Coal Mine Disaster Dynamics and Control, School of Resources and Safety Engineering, Chongqing University, Chongqing 400044, China

⁴School of Resources and Safety Engineering, Central South University, Changsha 410083, China

⁵China Urban Construction Design & Research Institute Co., Ltd, Beijing 100000, China

Correspondence should be addressed to Sen Tian; sentian@cqu.edu.cn

Received 23 June 2019; Accepted 17 September 2019; Published 31 October 2019

Academic Editor: Andrew R. Barron

Copyright © 2019 Linxing Zhang et al. This is an open access article distributed under the Creative Commons Attribution License, which permits unrestricted use, distribution, and reproduction in any medium, provided the original work is properly cited.

Sintering is an important approach for the alloying of different metals, which is affected by factors such as temperature, grain size, and material properties. And it represents a complex thermodynamic process. This paper had adopted the molecular dynamics methods to investigate the evolution process of nanostructure during the sintering of Cu and Au nanoparticles. The changes in crystalline during the nanosintering process were observed, and the radial distribution function of atoms, the shrinkage ratio, and the sintering neck of the systems were discussed. The initial sintering temperature and melting temperature of the system were obtained; at the same time, the characteristics of the sintering neck with changes in temperature during the nanosintering process were revealed.

1. Introduction

With the rapid development of manufacturing and processing industries, people have raised multiple performance requirements for equipment and materials, such as ultrahigh hardness, superb abrasion resistance, favorable heat resistance, sufficient toughness, and long-acting lifetime [1]. In the microelectronics field [2, 3], the electronic packaging materials have increasingly developed towards the direction of microminiaturization and high performance, and the dimension of the produced microscale solder joint has changed from millimeter level to microorder, and it is also the inevitable trend to develop towards the nanoscale ($1\text{ nm} = 10^{-9}\text{ m}$). Nanomaterials refer to the solids with nanoscale size in at least one direction [4]. Typically, their surface effect is far greater than that of bulk and microscale solids, which is ascribed to their huge specific surface area. As a result, they have distinctly different properties compared

with those of macroscopic substances. Meanwhile, as the most important part in electronic packaging technique, the reliability of solder alloy at nanoscale has attracted wide attention. As is well-known, the mechanical and thermal properties of nanoscale materials are obviously dependent on size, which is the phenomenon that cannot be observed in materials of conventional scale. Therefore, it is of great significance to investigate the various characteristics of nanoscale solder alloy, so as to analyze the lifetime reliability and the manufacturing process.

High-temperature electrically vacuum solders, which are mainly applied in electrical and electronic techniques, as well as microelectronics connection technology, have the basic characteristics of favorable wettability and mechanical-electrothermal properties. At present, the Au-based series solders are frequently used in electronically vacuum industry. Notably, the Au-Cu solders have relatively suitable melting point and pretty good mobility, which can also fill the fine

space. Most importantly, they possess favorable wettability for metals, such as Cu, Fe, Co, and W, together with their alloys [5, 6]. However, they are associated with the adverse defects such as hot crack and pore under moderate to high temperature (1400~1500 K), thus markedly reducing the joint mechanical performance. The huge surface energy effect makes it possible for low-temperature sintering of Cu/Au nanoparticles (NPs), which can thereby maintain the high-temperature electronically vacuum solders at the relatively high working temperature, optimize their thermomechanical coupling performance, and enhance their service life.

Generally, NPs have small size dimension, and their microscopic characteristics are distinctly different from the macroscopic ones. Consequently, they cannot be accurately observed and measured through the conventional experimental approaches. Molecular dynamics (MD) [7–12] simulation is an effective approach to simulate the atomic motion based on the Newtonian mechanics, which has been widely adopted by numerous scholars to examine the melting mechanism and sintering characteristics of Cu and Au NPs. For instance, Zhu and Averback [13, 14] investigated multiple Cu NP sintering processes and pointed out the important influence of grain boundary sliding on the sintering rate. Additionally, Arcidiacono et al. [15] used the theoretical model and MD methods to examine the sintering processes of Au NPs with various diameters, and their results underscored the dominant role of grain boundary diffusion in the sintering process of Au NPs at the size of over 2 nm. Li et al. [16] investigated the sintering processes of Cu NPs under various heating rates, and their results suggested that the initial sintering temperature [17] was dependent on the heating rate. Besides, Zeng et al. [18] examined the effects of six typical grain diffusion mechanisms on the sintering process. Taken together, the above studies have comprehensively summarized the sintering process of Cu and Au monomer NPs. However, the temperature-related parameters and microscopic mechanisms during their alloying processes have not been further investigated yet.

In this paper, Cu and Au NPs were used as the objects of the study, to investigate the connection mechanism, melting mechanism, and neck variation rule during their alloying process using the MD simulation method, which provided guidance for the variation trends of connection temperature and melting temperature during the process of low-temperature sintering.

2. Model and Simulation Details

2.1. Simulation Model. In this paper, the large-scale atomic/molecular massively parallel simulator (LAMMPS [19]) was utilized for MD simulation, and the embedded atom method (EAM) potential [20–22] was utilized for describing atom interactions within the systems. The EAM potential energy between atoms was expressed as follows.

$$\Phi = \frac{1}{2} \sum_{i \neq j} \varphi(r_{ij}) + \sum_i F(\rho_i), \quad (1)$$

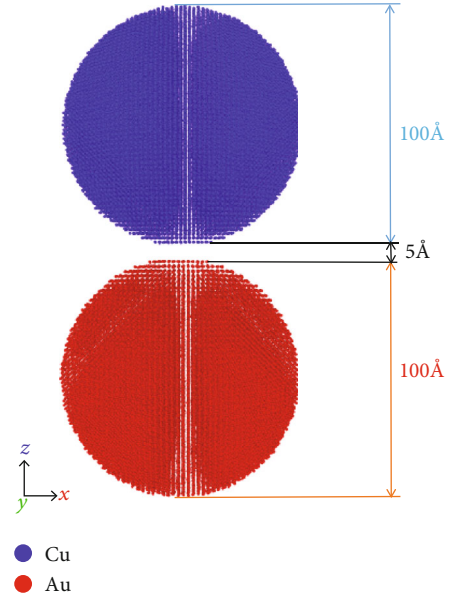


FIGURE 1: The model for sintering of Cu/Au nanoparticles.

where the first item is the two-body potential, F represents the embedded function, ρ_i stands for the electron density of i atom, while $\rho_i = \sum_j \rho(r_{ij})$, $\rho(r_{ij})$ is the electron density function. Among them, F and ρ have contained multiple specific parameters, which can be determined through fitting the known experimental data, such as elastic constant, equilibrium lattice constant, bulk modulus, and vacancy formation energy. The EAM potential parameter of Cu/Au adopted in this paper had been verified in our previous research [16, 23].

As shown in Figure 1, the simulation system in this paper was constituted by the 10 nm Cu NPs (a total of 44330 Cu atoms) and the 10 nm Au NPs (a total of 30875 Au atoms), the initial structure was the face center cubic (FCC) structure, and the initial distance between two NPs was 5 Å (1 Å = 10^{-10} m). The dimension of the simulation box was $252.7 \times 252.7 \times 252.7 \text{ \AA}^3$. More details about the construction of the initial model were described elsewhere [16].

2.2. Computational Parameters. The periodic boundary conditions were adopted at the X, Y, and Z directions, which corresponded to the crystal orientations of [1,0,0], [0,1,0], and [0,0,1], respectively [24, 25]. The time step of the system was set at 1 fs (1 fs = 10^{-15} s); specifically, the system was relaxed for 1,000,000 steps at room temperature ($T = 300$ K) in the NVT ensemble; subsequently, the temperature was linearly increased to 1700 K at the heating rate of 350 K/ns within 4,000,000 steps. The Nosé-Hoover algorithm was employed for temperature control in the simulations [26] with the damping parameter of 100 fs. Ovito [27], the open visualized software, was employed to analyze the crystal form changes during the entire sintering process.

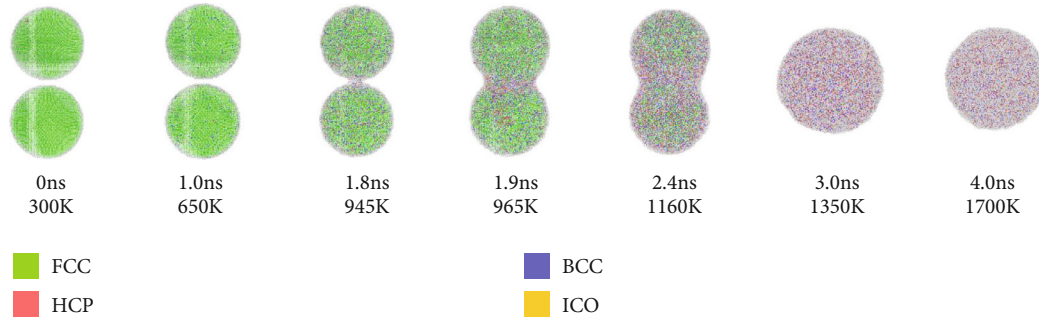


FIGURE 2: The alloying process for sintering of Cu/Au nanoparticles.

3. Results and Discussion

3.1. Alloying Process of Cu/Au NPs. Figure 2 shows the lattice evolution of the Cu/Au NPs during the alloying process. As could be observed, two particles with identical diameter maintained the intact FCC structure under ambient temperature, which was destroyed as the temperature increased. With the aggravation in atomic thermal vibration, these two NPs attracted mutually as a result of the huge surface energy, thereby reducing the mutual distance. When these two NPs became close to each other, they rotated to search for the binding crystal face that had the lowest contact energy. Specifically, they contacted each other under the action of adhesion at the temperature of about 945 K. Noteworthy, the contact process was dynamic and continuous, but it was difficult to define the contact temperature, so 945 K was generally defined as the initial sintering temperature T_{is} .

Thereafter, the compressive stress between these two NPs widened the contact part; in other words, the sintering neck was enlarged [28]. The vacancy migration direction during the sintering process was consistent with the direction of the reduced vacancy concentration [29].

$$\Delta C_V = C_{V0} \left[\exp\left(-\frac{\gamma\kappa\Omega}{KT}\right) - 1 \right], \quad (2)$$

where C_V represents the difference in vacancy concentration (difference in the vacancy concentration between the sintering neck surface and within the nanoparticle), C_{V0} stands for the vacancy concentration at the surface curvature of κ , γ is indicative of the material surface energy, Ω suggests the atom volume, K indicates the Boltzmann constant, and T is the absolute temperature.

According to equation (2), there was a negative curvature in the sintering neck, suggesting that the vacancy concentration on the sintering neck surface was higher than that within the nanoparticle, so the atoms moved along the opposite direction of vacancy migration. In other words, the atoms moved along the internal nanoparticle to the sintering neck surface, thus enlarging the sintering neck. As displayed in Figure 2, the neck growth rate was rather fast at the initial neck formation stage ($T = 945 \text{ K} - 965 \text{ K}$); thereafter, the neck growth rate became slower and even relatively stable, since the sintering rate was in direct proportion to the excess sur-

face area. Based on equation (3), the excess surface area became smaller and smaller as the neck dimension increased, and the sintering rate was gradually reduced until a balance was reached [30].

$$\frac{da}{dt} = -\frac{1}{\tau}(a - a_s), \quad (3)$$

where a is the total surface area at the sintering time of t , τ stands for the characteristic sintering time, and a_s demonstrates the total surface area of the nanoparticle after sintering.

When the temperature reached about 1160 K, the dimension of the sintering neck would be rapidly increased under the action of NP surface melting. At this moment, the FCC structure in the entire system was no longer dominant, while the number of amorphous structure was rapidly increased, indicating that the entire system had begun melting. At the temperature of about 1350 K, the entire system melted, because the melting point of the Cu/Au alloy bulk was reached, and the two NPs fused to form the new NP with the diameter of about 12.6 nm ($d_0 = 1.26d$) [31].

3.2. Initial Sintering Temperature and Melting Temperature

3.2.1. Melting Temperature (T_m). The melting mechanism plays a critical role in the sintering process, while the melting temperature is the temperature at which the entire system begins to melt. To obtain the melting temperature of the system, this paper applied the radial distribution function (RDF) to determine the melting temperature of the Cu/Au alloy NPs [32].

$$G(r) = \frac{dN}{\rho 4\pi r^2 dr}, \quad (4)$$

where N indicates the total particle number, ρ represents the ratio of local particle density to the average density, and $G(r)$ suggests the RDF at the distance of r away from the specific particle.

According to equation (4), the RDF described the occurrence probability of other particles around the coordinates of a specific particle within a certain range (cutoff radius), which was used to describe the particle orderliness. As observed from Figure 3, the different color curves represented

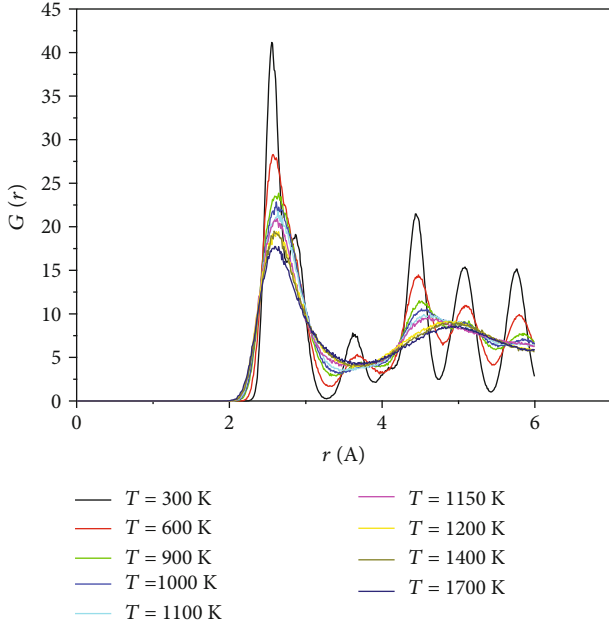


FIGURE 3: The curve of RDF variation with temperature during the Cu/Au sintering-alloying process.

the system RDF values at various temperatures. Typically, the cutoff radius value was set at 6 Å, suggesting that only the interactions between particles within the 6 Å range of a specific particle were taken into consideration. The interlayer spacing of the spherical shell was 0.01 Å, indicating that the particle distribution within that spherical shell should be calculated at an interval of 0.01 Å. At $T = 300$ K, the RDF displayed 5 relatively ordered peaks, demonstrating that all particles in the entire system were orderly arranged at this moment. However, these 5 peaks were markedly reduced as the temperature elevated. Noteworthily, the third peak was decreased again and then tended to be gentle, while the entire RDF values showed that the overall trend of atoms was ordering at the short range whereas disordering within the long range, revealing that the particles under such temperature entered the disordering status (melting status).

According to Figure 4, the magnified curve graph of the third RDF peak with temperature clearly displayed its variation trend; as a result, the melting temperature T_m was determined. Specifically, the 9 curves in different colors from the top to the bottom represented the RDF curves at the temperature of $T = 300$ K to $T = 1700$ K, and the value of the third peak was reduced as the temperature increased. In addition, the flat degree of curve (disordering) was also enhanced with the increase in temperature. At $T = 1200$ K and $T = 1700$ K, the same flat degree occurred near the third peaks of the three curves, indicating that the system showed the disordered state within such a temperature range (the melting state). At $T = 1150$ K, the curve showed distinctly different states from the those of the above three curves, which revealed that the system had not reached the melting state at that temperature. To sum up, the melting temperature of the present Cu/Au alloy NPs should be set within the range of $T = 1150$ K to $T = 1200$ K, which was consistent with the 1160 K obtained previously.

3.2.2. Initial Sintering Temperature (T_{is}). The initial sintering temperature refers to the system temperature at which the particles contact and connect with each other [33]. The entire system density begins to exponentially increase when the particles begin to contact each other [34, 35]; meanwhile, the spacing between particles also begins to shrink, while the macroscopic substance intensity and hardness are closely correlated with the connection tightness degree between particles.

Within the dozens of picosecond ($1 \text{ ps} = 10^{-12} \text{ s}$) when the particles began to contact each other, the distance between particles was first rapidly reduced during the entire sintering process. As a result, the shrinking ratio was used to determine the range of the particle initial sintering temperature. As shown in Figure 5, the black full line represented the variation curve of shrinkage ratio with temperature.

The distance between particles was defined as the distance between the mass centers of two NPs, which was 105 Å under the initial condition (Figure 1). The shrinkage ratio was calculated as follows [36].

$$\xi = \frac{D - D_{\text{com}}}{D}, \quad (5)$$

where D stands for the distance between the mass centers of two NPs at $T = 300$ K, and D_{com} indicates the real-time distance between the mass centers of two NPs.

According to Figure 5, the shrinkage ratio with the changing temperature during the entire nanoparticle sintering process experienced two vertical rising processes (3~4, 5~6); among which, the first vertical rising process (3~4) was closely correlated with the particle initial sintering. Within the temperature range of 300 K-945 K, the relative distance between particles remained almost unchanged. However, when the temperature reached about 945 K, the particles suddenly contacted each other, and the shrinkage ratio vertically increased immediately due to the great effect of surface energy until the temperature reached 965 K. In conclusion, the initial sintering temperature range was 945 K-965 K, and the initial sintering temperature was finally determined to be about 945 K, which was consistent with the 945 K obtained in the previous study.

3.3. The Sintering Neck. The sintering neck is an important product during the nanoparticle sintering process, which is the inevitable consequence of the coupling effect of surface curvature gradient and vacancy concentration gradient. Specifically, the sintering neck begins with the mutual contact between particles and ends up with the elimination of the NP surface curvature concentration gradient, as demonstrated in [37]

$$\sigma = \gamma\kappa = \gamma \left(\frac{1}{R_1} + \frac{1}{R_2} \right). \quad (6)$$

Among which, σ is the sintering driving force, γ stands for the material surface energy, and κ represents the surface curvature.

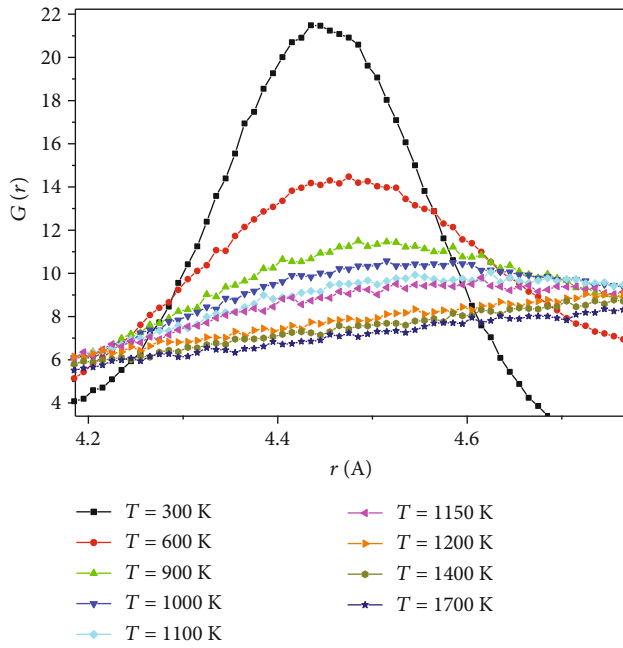


FIGURE 4: The curve of RDF variation with temperature during the Cu/Au sintering-alloying process (enlarged drawing for the third peak value).

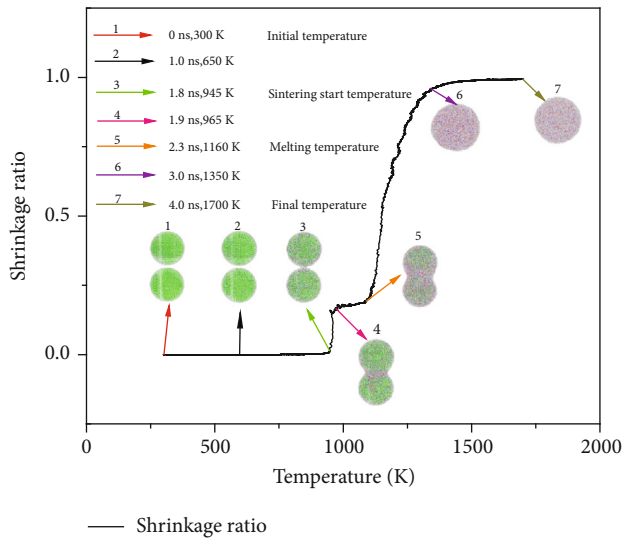


FIGURE 5: The curve of shrinkage ratio variation with temperature during the Cu/Au alloying process.

Equation (6) shows the additional pressure difference on the irregular surface during the sintering process, which also represents the sintering driving force. According to Figure 6, there were corresponding curvature radii of each curvature on the sintering neck and surface. Nonetheless, the irregular and uneven surface resulted in the production of additional pressure difference σ ; as a result, the convex surface (particle surface) was subjected to the compressive pressure, while the concave surface (sintering neck surface) was susceptible to the pulling stress. It was the natural trend that substance flowed from the high curvature region to the low curvature

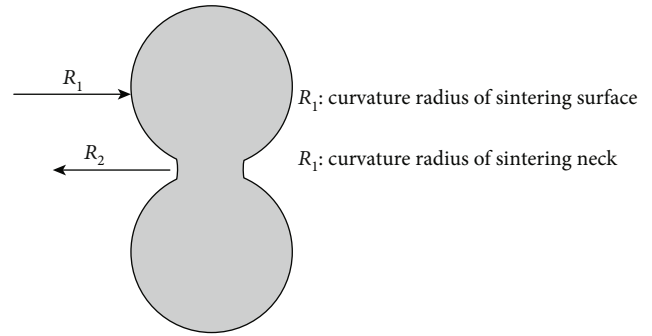


FIGURE 6: Curvature radius of sintering surface and neck.

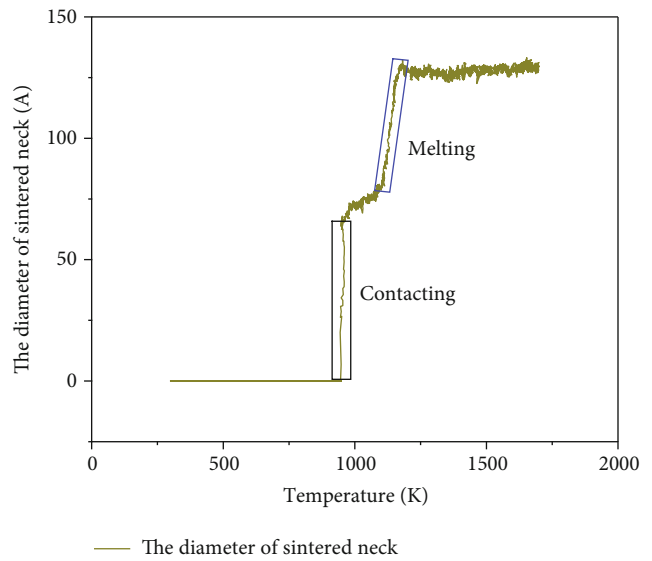
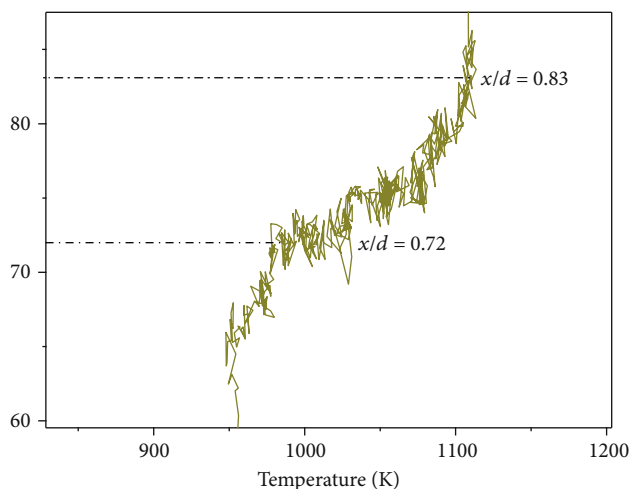


FIGURE 7: The curve of diameter of sintered neck variation with temperature.

region, which thereby resulted in the elimination of surface curvature concentration gradient, finally leading to the increase in the sintering neck dimension. It was shown in Figure 7 that the curve within the range of the black rectangular frame showed a vertically increasing trend, suggesting that the dimension of the sintering neck was enlarged rapidly within a short period of time. Obviously, such phenomenon was correlated with the action of the pressure difference σ .

Thereafter, the system experienced about 0.5 ns of the relatively stable stage (Figure 2). Noteworthy, the diameter ratio of sintering neck to NPs (x/d) ranged from 0.72 to 0.83 (Figure 8), which was identical with the findings by Kobata et al. [37], thus verifying the reliability of our MD simulation. When the temperature reached the melting point of NPs, the sintering neck became larger due to the action of spheroidization produced by NP melting, until two NPs fused into a greater NP ($d_0 = 1.26d$). According to Figure 9, the final alloy particle volume was equal to the sum of the initial volumes of the isovolumetric Cu and Au NPs. Then, $d_0 = d$ was deduced based on the mathematical formula, which was the above-mentioned 1.26-fold relationship.



— The diameter of sintered neck

FIGURE 8: The ratio of the diameter of the sintered neck variation to the diameter of the nanoparticle at the stable stage.

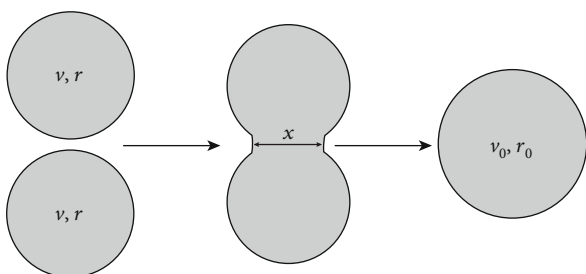


FIGURE 9: The shape evolution of two identical nanoparticles during sintering.

4. Conclusions

In this study, the Cu/Au nanoparticle alloying process is investigated; the temperature characteristics of the system and the variation rule of the sintering neck with temperature are also analyzed. The FCC structure of the system transforms into the amorphous structure with the increase in temperature. During the contact and melting process of these two NPs, the sintered neck diameter has experienced two vertical growths with the changing temperature. The vacancy concentration on the sintering neck surface is higher than that within the NPs, which results in the rapid growth of the sintering neck at the initial neck formation period. Additionally, the additional pressure difference between the convex surface and concave surface of the sintering system leads to the rapid growth of the sintering neck during the melting process. Besides, the system melting temperature is preliminarily determined to be 1160 K based on the RDF of atoms at different temperatures. The initial sintering temperature range of the system is determined to be about 945 K, which can be identified by the shrinkage ratio variation with temperature.

Data Availability

No data were used to support this study.

Conflicts of Interest

The authors declare no conflict of interest.

Authors' Contributions

L.Z. (Linxing Zhang) and G.H. (Guang Hong) participated in the design of the work, methodology, data interpretation, and analysis for the work; carried out the statistical analyses; and drafted the manuscript. Q.L. (Qibin Li) and S.T. (Sen Tian) designed the study; participated in the data interpretation, analysis for the work, and methodology; carried out the statistical analyses; and drafted the manuscript.

Acknowledgments

The authors would like to acknowledge the colleagues from the State Key Laboratory of Coal Mine Disaster Dynamics and Control for their perspectives and suggestions related to experimental study and data analyses. This research is supported by the National Natural Science Foundation of China (51904040 and 51876015), the Chongqing Research Program of Basic Research and Frontier Technology (cstc2018jcyjAX0522), the Program for Changjiang Scholars and Innovative Research Team in University (IRT_17R112), and the Innovation Support Program for Chongqing Overseas Returnees (cx2018071).

References

- [1] J. Koehler, "Attempt to design a strong solid," *Physical Review B*, vol. 2, pp. 547–551, 1970.
- [2] P. Rosa, T. G. Karayiannis, and M. W. Collins, "Single-phase heat transfer in microchannels: the importance of scaling effects," *Applied Thermal Engineering*, vol. 29, pp. 3447–3468, 2009.
- [3] J. Zhao, Q. Yuan, H. Sun, J. Yang, and L. Sun, "Stability characterization of vacuum encapsulated MEMS resonators with Au–Sn solder bonding," *Microsystem Technologies*, vol. 24, pp. 3885–3892, 2018.
- [4] H. Gleiter, "Nanostructured materials: state of the art and perspectives," *Nanostructured Materials*, vol. 6, pp. 3–14, 1995.
- [5] D. Easton, Y. Zhang, J. Wood, A. Galloway, M. O. Robbie, and C. Hardie, "Brazing development and interfacial metallurgy study of tungsten and copper joints with eutectic gold copper brazing alloy," *Fusion Engineering and Design*, vol. 98–99, pp. 1956–1959, 2015.
- [6] P. Shen, Y. Gu, N.-N. Yang, R.-P. Zheng, and L.-H. Ren, "Influences of electric current on the wettability and interfacial microstructure in Sn/Fe system," *Applied Surface Science*, vol. 328, pp. 380–386, 2015.
- [7] D. Frenkel and B. Smit, *Understanding Molecular Simulation: From Algorithms to Applications (Second Edition)*, Academic Press, New York, 2002.
- [8] Q. Li, Y. Xiao, X. Shi, and S. Song, "Rapid evaporation of water on graphene/graphene-oxide: a molecular dynamics study," *Nanomaterials*, vol. 7, p. 265, 2017.

- [9] Y. Liu and X. Chen, "High permeability and salt rejection reverse osmosis by a zeolite nano-membrane," *Physical Chemistry Chemical Physics*, vol. 15, pp. 6817–6824, 2013.
- [10] Y. Zhou, Q. Li, and Q. Wang, "Energy storage analysis of UIO-66 and water mixed nanofluids: an experimental and theoretical study," *Energies*, vol. 12, no. 13, p. 2521, 2019.
- [11] H. Zhan and Y. Gu, "A fundamental numerical and theoretical study for the vibrational properties of nanowires," *Journal of Applied Physics*, vol. 111, p. 124303, 2012.
- [12] L. Zhang, S. Tian, and T. Peng, "Molecular simulations of sputtering preparation and transformation of surface properties of Au/Cu alloy coatings under different incident energies," *Metals*, vol. 9, p. 259, 2019.
- [13] H. Zhu and R. S. Averback, "Molecular dynamics simulations of densification processes in nanocrystalline materials," *Materials Science and Engineering: A*, vol. 204, pp. 96–100, 1995.
- [14] H. Zhu, "Sintering processes of two nanoparticles: a study by molecular dynamics simulations," *Philosophical Magazine Letters*, vol. 73, pp. 27–33, 1996.
- [15] S. Arcidiacono, N. R. Bieri, D. Poulikakos, and C. P. Grigoropoulos, "On the coalescence of gold nanoparticles," *International Journal of Multiphase Flow*, vol. 30, pp. 979–994, 2004.
- [16] Q. Li, M. Wang, Y. Liang et al., "Molecular dynamics simulations of aggregation of copper nanoparticles with different heating rates," *Physica E: Low-dimensional Systems and Nanostructures*, vol. 90, pp. 137–142, 2017.
- [17] Q. Jiang and F. G. Shi, "Size-dependent initial sintering temperature of ultrafine particles," *Journal of Materials Science & Technology*, vol. 14, pp. 171–172, 1998.
- [18] P. Zeng, S. Zajac, P. C. Clapp, and J. A. Rifkin, "Nanoparticle sintering simulations," *Materials Science and Engineering: A*, vol. 252, pp. 301–306, 1998.
- [19] S. Plimpton, "Fast parallel algorithms for short-range molecular dynamics," *Journal of Computational Physics*, vol. 117, pp. 1–19, 1995.
- [20] M. S. Daw and M. I. Baskes, "Embedded-atom method: derivation and application to impurities, surfaces, and other defects in metals," *Physical Review B*, vol. 29, pp. 6443–6453, 1984.
- [21] S. M. Foiles, M. I. Baskes, and M. S. Daw, "Embedded-atom-method functions for the fcc metals Cu, Ag, Au, Ni, Pd, Pt, and their alloys," *Physical Review B*, vol. 33, pp. 7983–7991, 1986.
- [22] S. Cai, Q. Tang, S. Tian, Y. Lu, and X. Gao, "Molecular simulation study on the microscopic structure and mechanical property of defect-containing sI methane hydrate," *International Journal of Molecular Sciences*, vol. 20, no. 9, p. 2305, 2019.
- [23] Q. Li, X. Peng, T. Peng, Q. Tang, X. Zhang, and C. Huang, "Molecular dynamics simulation of Cu/Au thin films under temperature gradient," *Applied Surface Science*, vol. 357, no. - Part B, pp. 1823–1829, 2015.
- [24] J. Hu, C. Liu, Q. Li, and X. Shi, "Molecular simulation of thermal energy storage of mixed CO₂/IRMOF-1 nanoparticle nanofluid," *International Journal of Heat and Mass Transfer*, vol. 125, pp. 1345–1348, 2018.
- [25] Z. Rao, S. Wang, and F. Peng, "Molecular dynamics simulations of nano-encapsulated and nanoparticle-enhanced thermal energy storage phase change materials," *International Journal of Heat and Mass Transfer*, vol. 66, pp. 575–584, 2013.
- [26] D. J. Evans and B. L. Holian, "The Nose–Hoover thermostat," *The Journal of Chemical Physics*, vol. 83, p. 4069, 1985.
- [27] S. Alexander, "Visualization and analysis of atomistic simulation data with OVITO—the Open Visualization Tool," *Modelling and Simulation in Materials Science and Engineering*, vol. 18, article 015012, 2010.
- [28] P. Grammatikopoulos, C. Cassidy, V. Singh, and M. Sowwan, "Coalescence-induced crystallisation wave in Pd nanoparticles," *Scientific Reports*, vol. 4, p. 5779, 2014.
- [29] D. A. Porter, K. E. Easterling, and M. Sherif, *Phase Transformations in Metals and Alloys, (Revised Reprint)*, CRC Press, Boca Raton, 2009.
- [30] W. Koch and S. K. Friedlander, "The effect of particle coalescence on the surface area of a coagulating aerosol," *Journal of Colloid and Interface Science*, vol. 140, pp. 419–427, 1990.
- [31] Y. Zhang, L. Wu, H. El-Mounayri, K. Brand, and J. Zhang, "Molecular dynamics study of the strength of laser sintered iron nanoparticles," *Procedia Manufacturing*, vol. 1, pp. 296–307, 2015.
- [32] Q. Li, C. Liu, and X. Chen, "Molecular characteristics of dissociated water with memory effect from methane hydrates," *International Journal of Modern Physics B*, vol. 28, article 1450062, 2014.
- [33] M. I. Alymov, E. I. Maltina, and Y. N. Stepanov, "Model of initial stage of ultrafine metal powder sintering," *Nanostructured Materials*, vol. 4, pp. 737–742, 1994.
- [34] Z. Z. Fang and H. Wang, "Densification and grain growth during sintering of nanosized particles," *International Materials Reviews*, vol. 53, pp. 326–352, 2008.
- [35] M. Alymov and Y. Stepanov, "Coagulation and coalescence in ultrafine metal powders," *Journal of Aerosol Science*, vol. 26, pp. S811–S812, 1995.
- [36] P. Song and D. Wen, "Molecular dynamics simulation of the sintering of metallic nanoparticles," *Journal of Nanoparticle Research*, vol. 12, pp. 823–829, 2010.
- [37] A. Kobata, K. Kusakabe, and S. Morooka, "Growth and transformation of TiO₂ crystallites in aerosol reactor," *AIChE Journal*, vol. 37, pp. 347–359, 1991.



Hindawi
Submit your manuscripts at
www.hindawi.com

